Testing and improving the redox stability of Ni-based solid oxide fuel cells

M. Pihlatie [a,b,*], T. Ramos [a], A. Kaiser [a]

[a] Risoe National Laboratory for Sustainable Energy, Technical University of Denmark, P.O. Box 49, DK-4000 Roskilde, Denmark
[b] Helsinki University of Technology, Department of Engineering Physics, P.O. Box 4100, FI-02015 TKK, Finland

ARTICLE INFO

ABSTRACT

Despite active development, solid oxide fuel cells (SOFCs) based on Ni-YSZ anodes still suffer from thermomechanical instability under conditions where the anode side is exposed to oxidising conditions at high temperature. In the first part of the paper, structures and solutions, which could improve the redox stability of Ni-YSZ anode supported SOFC's in terms of dimensional and mechanical stability are reported. Porosity is identified as a major microstructural parameter linked to the dimensional and structural stability during redox cycling. The cumulative redox strain (CRS) after three isothermal redox cycles at 850 °C increases by a factor of more than 20 when the as-sintered porosity of the composites is reduced from 34 to 9%. The effect of reduction and redox cycling on the Ni-YSZ anode are discussed in light of electrochemical measurements using impedance spectroscopy on symmetric cells. When the symmetric cells are reduced and redox cycled isothermally at 850 °C, no major change in the serial or polarisation resistance of the cell and electrodes was measured. When the cells are, after the similar initial reduction treatment, redox cycled at 650 °C, the serial resistance remains almost unchanged but the polarisation resistance decreased by about 60%.

© 2009 Published by Elsevier B.V.

1. Introduction

Solid oxide fuel cells (SOFCs) continue to be a promising energy conversion technology for environmentally benign power generation, capable of utilising different hydrocarbons as well as hydrogen as the fuel [1]. Despite active search for alternatives such as fully ceramic or nickel-free anodes, Ni-YSZ composites are still widely used fuel electrodes [2–4]. Such cermets often also serve as structural materials for the electrochemical devices, either in planar or tubular designs. A generally known drawback of the Ni-based cells is that they are susceptible to thermomechanical instability when the anode side is exposed to oxidising conditions at high temperature. While many of the fundamental degradation mechanisms of the SOFC are currently known and strategies exist on how to overcome them, the problem of redox stability remains as a one of the cumbersome tasks [5]. Oxidation of the Ni contained within the porous composite into NiO entails a substantial volumetric expansion that exerts large stresses on the ceramic backbone of the composite. The re-oxidation of an operating cell can lead to mechanical rupture, leaks, and in the worst case a catastrophic failure of the SOFC. The solutions to the redox stability problem of SOFC can be approached at many levels: with SOFC system control and design, by design of cell and stack geometry, or through materials selection as well as optimisation of the microstructure and composition of the anode half cell. The optimal and most cost effective way to design the cell, the stack and the system depends on several factors such as system size, typical or required load profiles and the level of safety and automation systems. For example, elaborate safety or purge gas systems may not be affordable in small scale systems and therefore the durability of the cell itself plays a central role. To circumvent the redox stability problems in practical SOFC systems, the optimal solution is to have a system composed of robust, redox stable cells that can withstand partial or even full re-oxidation without significant losses to their functionality.

Different strategies to mitigate the redox instability at cell level, that is, of a single repeating unit (SRU), comprise geometrical design of the cell, materials selection and microstructural design of the structural components. Geometrically, both the "1st generation" thick electrolyte supported cell and the micro-tubular SOFC are more robust to thermal or redox cycling as compared to the thin electrolyte anode supported cell [6–9]. On anode supported electrolyte (ASE) SOFC, Wood et al. discussed different approaches to improve redox stability [10]. On the selection of materials, novel compositions such as fully ceramic Ni-free anodes, e.g. [11], are being developed, but their technological viability in terms of reproducibility, durability and cost remains to be proven. The redox properties of an ASE cell based on Ni-YSZ can be tackled through processing by variations in microstructure and composition. The impact of microstructure on the stability of Ni-YSZ cermets has been addressed in thermomechanical, dimensional and kinetics studies.

* Corresponding author. Present address: VTT Technical Research Centre of Finland, P.O. Box 1000, FI-02044 VTT, Finland. Tel.: +358 45 1103464/400 430395; fax: +358 20 7227048.
E-mail addresses: mikko.pihlatie@iki.fi, mikko.pihlatie@vtt.fi (M. Pihlatie).

Both Itoh et al. and Waldbillig et al. report that they have found more stable structures when implementing composites with coarser particles [12,13]. Even though the coarser phase for Itoh et al. was zirconia and for Waldbillig it was Ni/NiO, the basic effect of this modification is likely to be the same, that is, to slightly increase the porosity of the sample. Waldbillig et al. state the anticipated positive effect to redox stability from slightly reducing the Ni content; at the same time it must be ensured that sufficient Ni percolation remains [14]. It has been established by mechanical modelling that the ASE can withstand about 0.1–0.2% expansion of the supporting composite during redox cycling without cracking [7,15,16]. This level of dimensional stability of the supporting composite thus constitutes a suitable target level, which could enable an intact cell after a redox cycle without resorting to additional tricks such as functionally graded structures [14] or novel but more labour consuming manufacturing techniques like Ni infiltration [17].

Waldbillig et al. [14] investigated the effect from two functionally graded modifications: a twin-layered graded anode having less nickel in the layer next to the electrolyte to alleviate stress concentration, and a more dense (air) diffusion barrier layer at the backside of the anode support to slow down re-oxidation kinetics. The authors reported that both of these variations improved redox tolerance by reducing the electrochemical performance loss of the cell. Busawon et al. [17] report dimensional stability and fair electrical conductivity on pre-sintered porous YSZ backbones where 12–16 wt.% Ni was infiltrated into the YSZ structure. The challenge with this kind of approach is whether or not suitable and cost-effective techniques can be found for up-scaled production. Sarantaridis et al. [18] have shown the importance of the oxidation procedures for the thermomechanical behaviour and failure modes of the ASE cells. While the investigated cells could tolerate a Degree of Oxidation (DoO) of about 50% when exposed to air from the backside (anode side flow channels), an electrochemically driven oxidation by oxygen arriving across the electrolyte resulted in cell failure already at a DoO of about 5%. Therefore, the results indicate that a local (fast) oxidation in the anode–electrolyte interface where the anode is relatively dense is the worst operation mode of the cell and generates a stress peak at the electrolyte. This type of situation might arise e.g. on extreme cell loading with fuel utilisation approaching 100% when the local $p(O_2)$ could approach or exceed that needed for oxidation of Ni or, to a lesser extent, through fast communication of oxygen through the backside of the anode support to a more dense anode in a design where the anode support is very porous.

Besides the thermomechanical degradation and failure due to redox cycling of Ni-based ASE cells, the electrical and electrochemical effects are naturally of interest. The thermomechanical degradation of the Ni-YSZ cermet, detachment of the anode/electrolyte interface and failure of the electrolyte result in loss of electrochemical reaction sites, ionic conduction paths as well as loss of fuel, generally observed as performance loss of the cell. In many occasions, especially on full re-oxidation, the integrity of the ASE is lost so that the performance of the anode after the redox cycle is impossible to assess. The DC electrical conductivity of Ni-YSZ composites with coarse Ni has been reported to increase from 500 to 1000 S cm^{-1} upon a redox cycle at 850 °C by Grahl-Madsen et al. (the in-plane conductivity also given at 850 °C) [19]. Young et al. report an increase in DC electrical conductivity of Ni-YSZ anode support cermets as a function of redox cycles at 800 °C, whereas the conductivity in an anode composite, presumably having another microstructure decreased. The electrochemical performance of the anode improved on redox cycling at 800 °C for both the serial and polarisation resistance, as long as the ceramic backbone and the electrolyte remained intact [20].

The redox instability mechanism due to the sintering of nickel has been discussed by Klemensø et al. [21]. It has been demon-

strated that the dimensional stability on redox cycling is very dependent on the conditions under which the reduction and re-oxidation takes place. The main operation conditions affecting redox stability are temperature and humidity. Both of them affect the growth of Ni particles in the reduced state through particle coalescence and sintering. In addition to Ni sintering, the temperature of re-oxidation plays a significant role for the dimensional behaviour in that re-oxidation at high temperature (850 °C or above) leads to larger redox expansion [22,23]. Additionally, the dimensional changes and the resulting thermomechanical behaviour depend closely on the composite microstructure as will be shown in the present paper. While the supporting composite can be optimised for structural and dimensional stability, electrical conduction and gas transport, the anode itself has less free microstructural parameters to be modified since it should retain its good electrochemical performance. Therefore, we deem it justified to pursue examining both the dependence of the cermet dimensional response on some microstructural variations, and the effect of redox cycling as well as the temperature of redox cycling on the electrochemical performance of the anode with a typical microstructure. This paper addresses thermal analysis, including dimensional behaviour from dilatometry and reduction–oxidation kinetics from thermogravimetric analysis (TGA), of a few different processing variants of Ni-YSZ composites. The second part of the paper assesses the electrochemical performance and microstructure of symmetric cells with Ni-ScYSZ anodes, before and after redox cycling at different temperatures. In a related work, we plan to implement modified ASE cells and test them for redox stability in comparison with standard cells.

2. Experimental

2.1. Ni-YSZ cermets

The cermets tested were manufactured from commercial NiO and 3YSZ powders using standard ceramic processing techniques and equipment. The powders were ball milled in ethanol-based slurries using dispersants and organic binders. The green tapes were cut into a number of sibling pieces for use in either TGA or dilatometry, and sintered at 1300–1400 °C. The as-sintered sizes of the dilatometry samples were about 5 mm × 24 mm, while the TGA samples were about 5 mm × 15 mm with a Ø2.5 mm hole in one end. The thickness of the tested samples varied, depending on the thickness of the tape cast, between 0.3 and 0.8 mm. The baseline samples were similar to those reported in [22,23]. Different modified composites were prepared using the same ceramic processing route and by varying the particle size distributions of NiO and YSZ. The size distributions of powders were measured using a Beckman Coulter laser diffraction instrument. Table 1 shows the available open and total porosities of the samples. The open porosities were measured by mercury intrusion porosimetry using a Micromeritics instrument. The total porosities were determined by geometrical measurements for larger samples as described in [24]. The total porosities in the reduced state of the baseline samples are about 35–40%, for sample A about 29% and for the modified samples D–N up to about 52%. Different variants of the industrial grade NiO powder used comprised pre-milled uncalcined, calcined, and powder doped with secondary oxides of either Mg, Al or Ce. The secondary oxide coatings were implemented through application of oxide precursors during ceramic processing. It should be stressed that there are several overlapping processing parameters fundamentally affecting the as-sintered microstructure, porosity and subsequent redox stability of the composites. These parameters include the sintering time and temperature, the particle size distributions of the powders and the sintering characteristics of each powder or raw

Table 1
List of samples tested in dilatometry with details on Ni treatment, sintering, and porosity.

Sample name	Ni treatment	Sintering T (°C), 12 h	Total p (%)	Open p (%)
A	NiO	1300–1320	9[a]	7
B	NiO	1300–1320	14[a]	12
C—baseline	NiO	1300–1320	14	12
D	NiO	1350–1370	26	–
E	NiO	1300–1320	33	–
F	NiO	1300–1320	28	–
G	NiO calcined	1350–1370	31	–
H	NiO calcined	1320–1340	33	–
I	NiO + Al_2O_3	1350–1370	27	–
J	NiO + MgO	1350–1370	38	
K	NiO	1350–1370	34	–
L	NiO	1390–1410	30[b]	–
M	NiO + CeO_2	1350–1370	37	–
N	NiO + CeO_2	1390–1410	34[b]	–

[a] Estimated value based on the open porosity measurement.

[b] Determined from the smaller dilatometry sample, thus a less accurate value.

Fig. 1. Schematic of the electrochemical setup for symmetric cell testing.

material. In addition, particle shape, surface morphology and packing as well as the rheological quality of the colloidal suspension used also play a role.

Thermal analysis was carried out using a Netzsch 402 CD differential dilatometer for dimensional behaviour and a Netzsch STA 409 CD thermo gravimeter for studying the reduction–oxidation reaction. Both instruments were equipped with a gas control unit capable of programmed mixing of up to three different gases. The experimental approach was similar to that employed in [22,23], although only tests in dry gas were carried out. The dilatometer runs were identical in the thermal and gas change programmes, were obtained isothermally at 850 °C and comprised three redox cycles. The samples were exposed to an air flow in the following time intervals following the start of the initial reduction: 740–980, 1380–1620 and 2020–2260 min, which correspond to the 1st, the 2nd and the 3rd redox cycles, respectively. A 20 min flush of N_2 was implemented prior to each oxidising-reducing gas change. The gas flow was 100 ml min^{-1} in all dilatometer tests and 100 ml min^{-1} air/N_2/9% H_2 in N_2 + 6 ml min^{-1} N_2 (sample gas plus gauging section protective gas) for the TGA experiments. The dimensional change due to redox cycling during the dilatometer experiments is expressed in terms of cumulative redox strain (CRS), which gives the accumulating length change of the dilatometer sample during redox cycling under isothermal conditions, relative to the initial cold state sample length, dL/L_o. Since the CRS curve typically shows a maximum peak value followed by relaxation as a function of time, the parameter CRS_{max} more specifically refers to the maximum length change as a function of redox cycling. The degree of redox reversibility (DRR) is a measure of how much of the strain induced by the re-oxidation is recovered upon subsequent re-reduction; the value of 1 indicates full strain reversibility during a redox cycle [22]. The degree of the reduction–oxidation reaction is expressed in terms of the weight fraction of Ni oxidised, DoO [23].

2.2. Symmetric cells

The impact of re-oxidation and re-reduction on anode performance and microstructure was evaluated by electrochemical impedance spectroscopy (EIS) and scanning-electron microscopy (SEM), using symmetric cells with anode. The tests were performed in specially designed rigs, which allow the evaluation of four symmetric cells per test run. A brief schematic of the test set-up can be seen in Fig. 1.

The cells were manufactured solely by tape-casting, and contained a Sc-doped YSZ (ScYSZ) thick electrolyte (~140 μm) and Ni-ScYSZ cermet anodes (~30 μm). After sintering at an appropri-
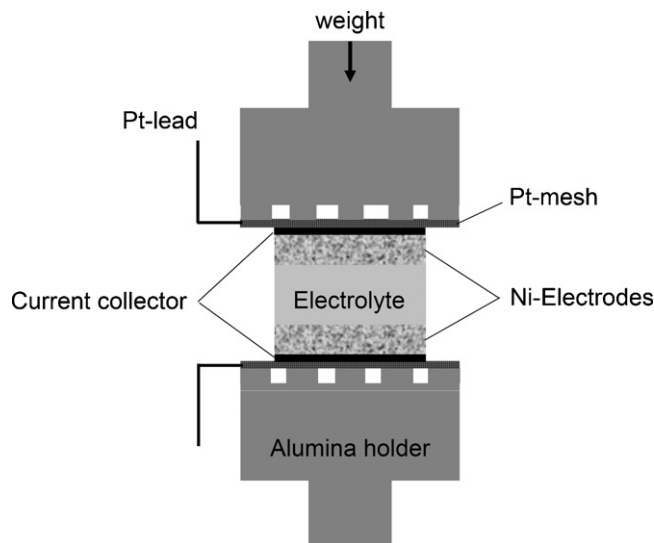
ate temperature, the samples were cut into 6 mm × 6 mm pieces and spray-painted with a Ni-YSZ slurry for current collection. Two independent tests were performed, A and B, both following a similar test protocol during the initial stages (fingerprinting). Unless otherwise stated, all gas flows were 100 ml min^{-1} and all samples were allowed to equilibrate for a period of 30 min at each new temperature and/or gas atmosphere before EIS measurements were performed. The heating/cooling ramp was 1 °C min^{-1}. The cells were heated up in air to the nominal temperature of 1000 °C and allowed to equilibrate for 10 min before the air supply was stopped and the remnant air flushed out by a flow of N_2 for 30 min. At the end of the flush, a H_2 flow saturated in water at room temperature (~3% H_2O) was introduced and the samples reduced for 20 min. The furnace was then allowed to cool down to the nominal temperature of 850 °C and the first EIS measurements were performed. From this point onwards, test A and test B differ. In test A, normal fingerprinting was continued by cooling the furnace to the nominal temperatures of 750 and 650 °C. Following these measurements, the H_2 supply was stopped, the chamber flushed with N_2 and the air flow re-started for a period of 12 h at the nominal temperature of 650 °C. After a new N_2 flush, the 97% H_2 + 3% H_2O flow was re-introduced. The first EIS measurements were performed 120 min after the start of the re-reduction procedure. Another six sets of measurements were performed under the same conditions, at fixed intervals, in order to assess the impact of re-reduction time on the performance. The redox cycle in test B was the same as previously described for test A, but performed at the nominal temperature of 850 °C instead of 650 °C. Additional measurements were performed in test B at 650 °C for comparison with those obtained in test A at the same nominal temperature. An extra set of EIS measurements was performed, for both tests, at the nominal temperature of 300 °C, to check for electrolyte integrity. Following this final check, the samples were cooled down to room temperature in safety gas, i.e., 9% H_2 + N_2. A third test, reference test, was performed following the same procedure as that used for test A, but without the redox cycle, i.e. the samples were fingerprinted between 850 and 300 °C with no re-oxidation stage. All samples were then molded in epoxy, cut, ground and polished before inspection by electron microscopy.

The impedance measurements were performed at open circuit voltage (OCV) using a Solartron SI1260 impedance/gain phase analyser, with 24 mV amplitude, in the frequency range of 0.05 Hz to 1 MHz. The post-test microstructural analysis was performed on a Hitachi TM1000 Tabletop microscope. All impedance spectra were

corrected for inductance (typical values of 10^{-8} H) and used to extract the ohmic losses (R_s) and the total polarisation resistance (R_p). The R_s value corresponds to the high frequency intercept of the impedance with the real axis, whereas R_p corresponds to the difference between the high frequency intercept and the total resistance at the limit $f \rightarrow 0$ Hz. The R_s values were also corrected for pre-determined ohmic contributions arising from the Pt leads in the experimental setup.

3. Results

3.1. Ni-YSZ cermets

Fig. 2 shows backscattered electron (BE) micrographs using a JEOL LVSEM from polished cross-sections of as-sintered sample B. The dimensional behaviour during three isothermal redox cycles at 850 °C of selected Ni-YSZ composites, samples A–H, are shown in Fig. 3. The dimensional stability shows great differences; the CRS$_{max}$ after three redox cycles of the most unstable sample (A) is more than 20 times the CRS$_{max}$ of the most dimensionally stable one (sample H). The CRS$_{max}$ points for each of the three redox cycles from totally 14 different tests with undoped Ni, including those shown in Fig. 3,
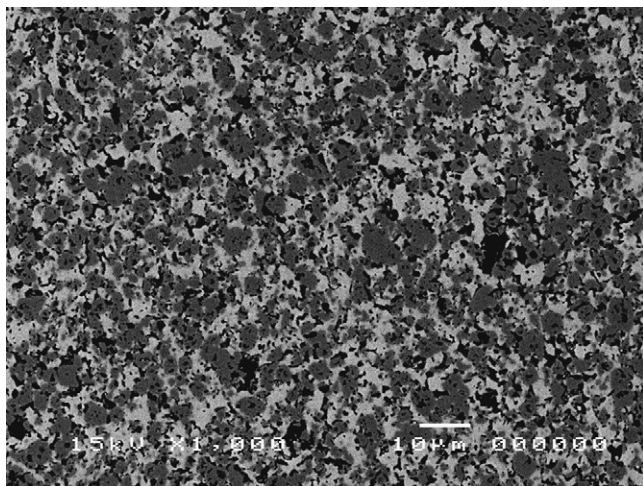
Fig. 2. Polished cross-section BE-SEM micrograph after sintering of sample B having a microstructure close to the baseline sample and undoped NiO. Darker gray is NiO, lighter gray is YSZ and black areas are porosity.
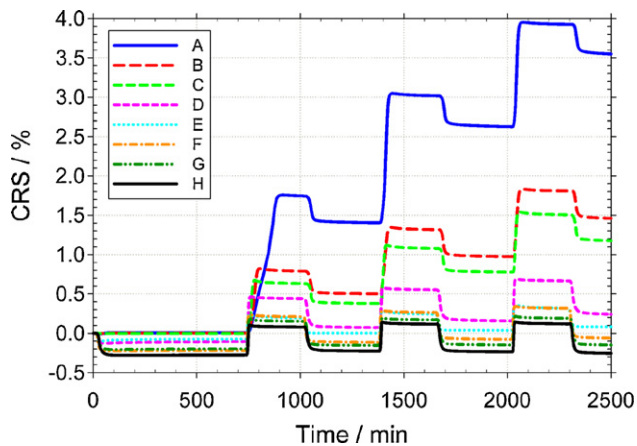

Fig. 3. Cumulative redox strain (CRS) as a function of time from the initial reduction during three isothermal redox cycles of different Ni-YSZ cermets at 850 °C. The zero-point on the CRS scale corresponds to the sample length prior to the initial reduction at the same nominal temperature.
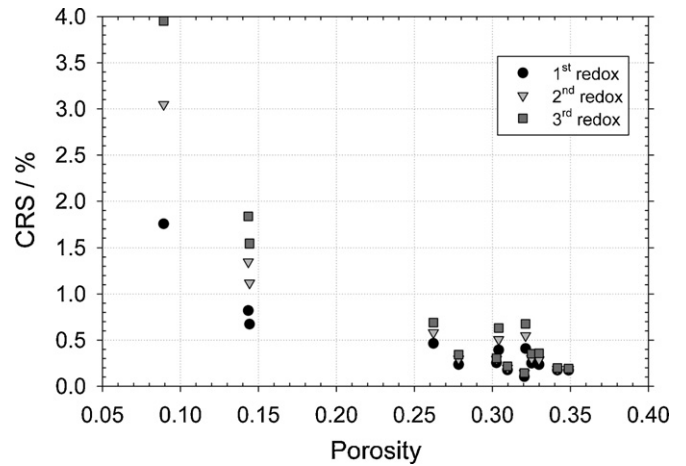

Fig. 4. Maximum cumulative redox strain (CRS$_{max}$) values obtained in isothermal redox cycling dilatometry comprising three redox cycles, as a function of estimated total porosity of different Ni-YSZ cermets.

are plotted in Fig. 4 as a function of the estimated total porosity of the samples. The DRR values pertaining to the same experiments are shown in Fig. 5. The most stable undoped cermets G and H have CRS$_{max}$ approaching the target value of 0.1%, and a DRR of close to unity. With decreasing porosity, the CRS$_{max}$ values increase and DRR decrease. Macroscopic damage and in some cases sample buckling could be visually observed after the three redox cycles in samples A–C. The higher porosity samples D–H were visually intact and straight after the redox experiments.

Fig. 6 shows results from isothermal dilatometry of Ni-YSZ composite samples G, I and J. In these variants the NiO treatment affected the sintering behaviour as can be observed from the geometrically estimated total porosities of the materials shown in Table 1. Fig. 7 shows the results from redox dilatometry of samples K–N. The deduced CRS and DRR values shown in Figs. 6 and 7 are collected in Table 2. The cermet with undoped NiO (sample G) in Fig. 6 show relatively stable CRS at around 0.2% and a DRR close to unity. The cermet with the Al-doped Ni (sample I) is slightly denser than the rest of the cermets with doped or calcined NiO in Table 1; this could be one reason for the DRR being lower than in the other cermets. The Mg-doped sample J shows the highest initial CRS, though it decreases with redox cycling; the DRR values are very high. In Fig. 7, the CRS of the Ce-doped sample M remained below the target level during the experiment with a minor decrease
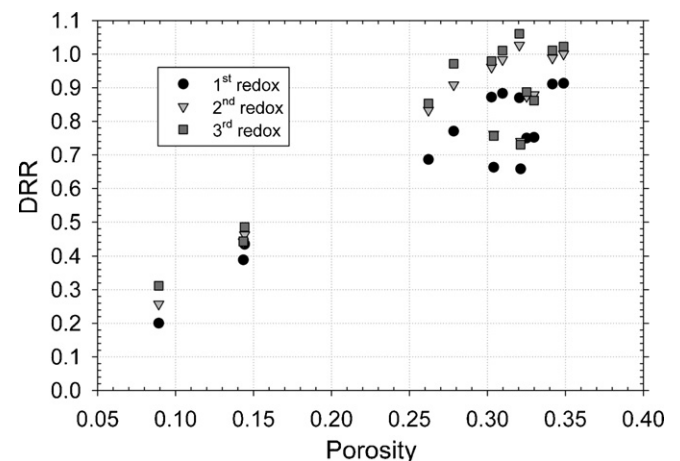

Fig. 5. The degree of redox reversibility (DRR) in isothermal redox cycling dilatometry comprising three redox cycles, as a function of estimated total porosity of different Ni-YSZ cermets.
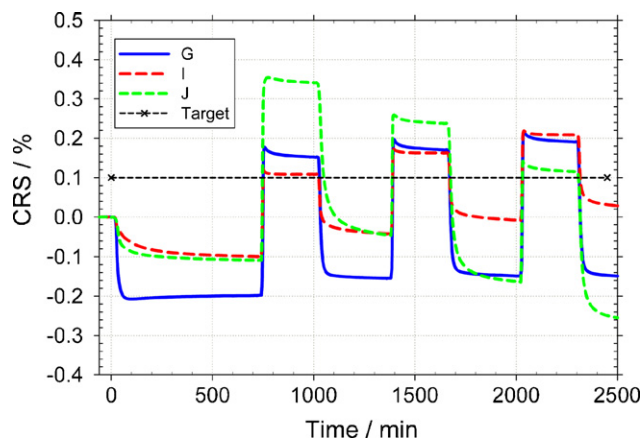
Fig. 6. Cumulative redox strain as a function of time from the initial reduction during three isothermal redox cycles at 850 °C of Ni-YSZ cermets with either pre-calcined NiO (sample G) or NiO doped with Al (sample I) or Mg (sample J). The zero-point on the CRS scale corresponds to the sample length prior to the initial reduction at the same nominal temperature.
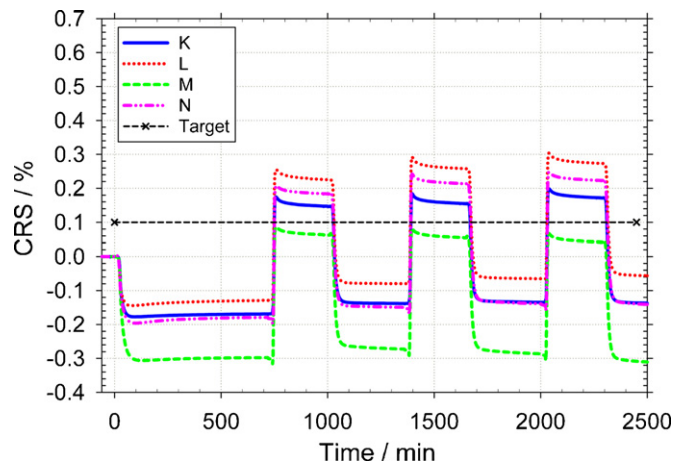

Fig. 7. Cumulative redox strain (CRS) as a function of time from the initial reduction during three isothermal redox cycles at 850 °C of Ni-YSZ cermets with either as-received NiO (samples K and L) or NiO doped with Ce (samples M and N), K and M sintered at 1350–1370, and L and N at 1390–1410 °C. The zero-point on the CRS scale corresponds to the sample length prior to the initial reduction at the same nominal temperature.

in CRS$_{max}$ on redox cycles, equal to the DRR being slightly in excess of unity. The CRS of the Ce-doped sample N was close to that of the undoped sample K with similar porosity, sintered at 1360 °C.

The dimensional response together with the DoO versus time of a NiO/Ni-YSZ composite with a typical baseline microstructure is shown in Fig. 8a for isothermal reduction and in Fig. 8b for isothermal re-oxidation at 850 °C for the sample previously reduced at
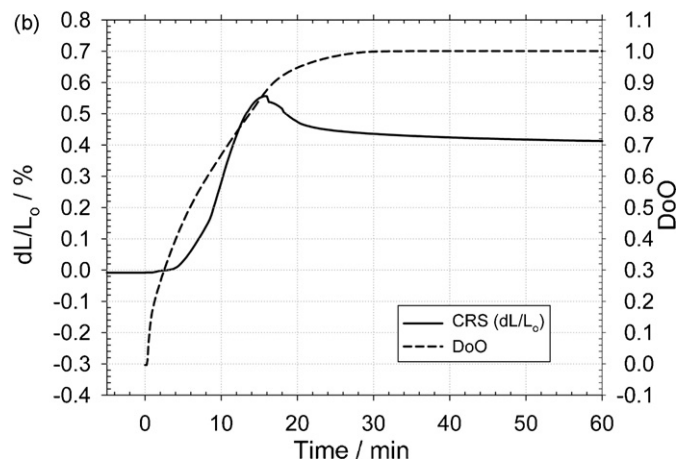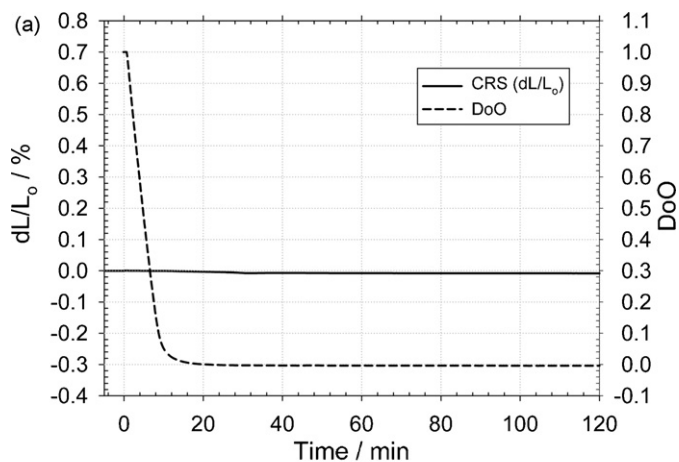

Fig. 8. Dimensional change due to the phase change and the degree of oxidation as a function of time of a Ni/NiO-YSZ composite with a typical baseline microstructure, during (a) isothermal reduction of an as-sintered sample, and (b) re-oxidation of a pre-reduced sample.

850 °C. The thickness of the TGA sample has been rescaled, affecting the time axis, to correspond to the thickness of the dilatometry sample as described in [23]. The dilatometry sample shown in Fig. 8b buckled at about 15 min into oxidation so that the final CRS$_{max}$ could not be measured, therefore also the decrease in the dL signal in Fig. 8b after 15 min is not related to thermomechanical relaxation, but due to the buckling of the sample. Nevertheless, the dL–DoO behaviour prior to the dilatometry sample buckling is relevant. Fig. 9 shows the dimensional behaviour and reaction kinetics of a NiO/Ni-YSZ composite with a modified microstructure and undoped Ni. Fig. 9a corresponds to isothermal reduction and Fig. 9b to isothermal re-oxidation of the reduced sample at 850 °C.

Table 2
The cumulative maximum redox strain CRS$_{max}$ and redox strain reversibility DRR as a function of the number of redox cycles of porous Ni-YSZ composites with different NiO variants.

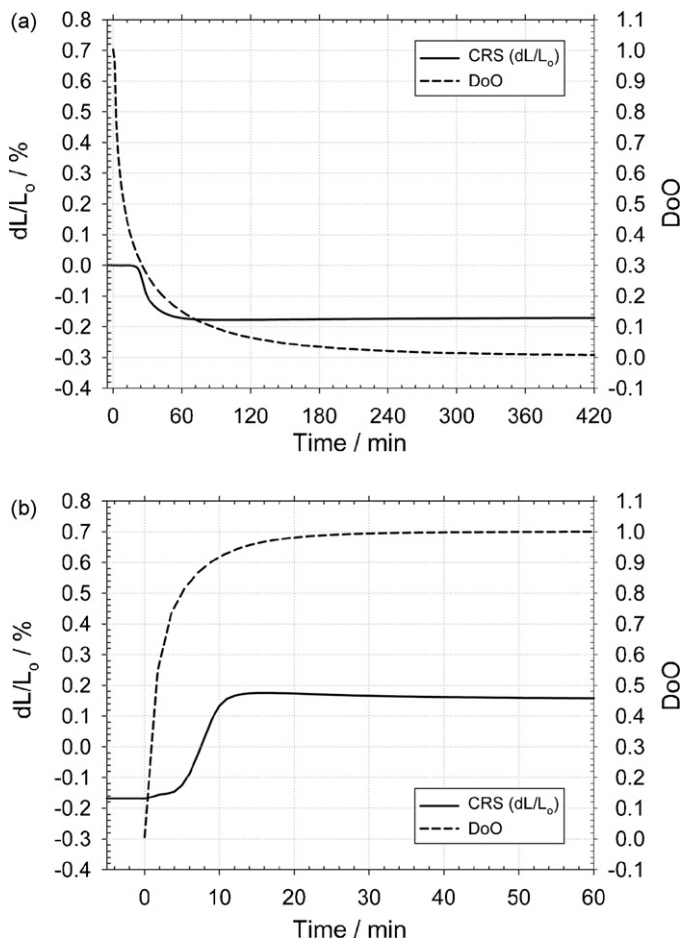| Sample	CRS$_{max}$ (%)			DRR		
	1st redox	2nd redox	3rd redox	1st redox	2nd redox	3rd redox
K (NiO uncalcined)	0.17	0.18	0.20	0.91	0.99	1.01
G (NiO calcined)	0.18	0.20	0.22	0.88	0.98	1.01
I (NiO + Al$_2$O$_3$)	0.12	0.17	0.22	0.74	0.84	0.86
J (NiO + MgO)	0.35	0.26	0.14	0.86	1.39	1.33
M (NiO + CeO$_2$)	0.09	0.08	0.07	0.93	1.04	1.08
L (NiO uncalcined)	0.25	0.29	0.30	0.87	0.96	0.98
N (NiO + CeO$_2$)	0.21	0.24	0.25	0.92	0.97	1.01

(a)

(b)

Fig. 9. Dimensional change due to the phase change and the degree of oxidation as a function of time of a Ni/NiO-YSZ composite with a modified microstructure, during (a) isothermal reduction of an as-sintered, and (b) re-oxidation of a pre-reduced sample.

3.2. Symmetric cells

Fig. 10 shows representative Nyquist plots of the recorded impedance data for test A and test B, while Figs. 11 and 12 show the variation of the determined area specific R_s and area specific R_p as a function of temperature. The results obtained for test A before the 12 h re-oxidation show the expected increase in both R_s and R_p with decreasing temperature. Also shown are the R_s and R_p obtained at 650 °C, approximately 10.2 and 18.2 h into the re-reduction process. These are approximately 60% lower ($0.45 \pm 0.01\,\Omega\,cm^2$ 10.2 h into re-reduction) than those obtained before re-oxidation, with no significant changes observed for R_s at the showed times. Test B, where the re-oxidation temperature was increased to 850 °C, exhibits a very different behaviour. At 10.2 h into the re-reduction process, the differences in R_p and R_s are negligible when compared to those before re-oxidation. Once cooled to 650 °C and compared to the values obtained at the same nominal temperature during fingerprinting in test A, i.e., before re-oxidation, significantly poorer anode performances can be seen for cells in test B. If Figs. 11 and 12 are examined, it is possible to see that very similar values of R_s and R_p are obtained during fingerprinting at 850 °C for both tests. Hence, poor cell reproducibility cannot account for the measured poorer performance. Also notice that the impact on R_p was significantly greater than that seen for R_s.

Fig. 13 shows the impact of re-reduction time on performance. The Nyquist plots of the recorded impedance data exemplify the behaviour for one cell for each test. In test A, 2.2 h after the start
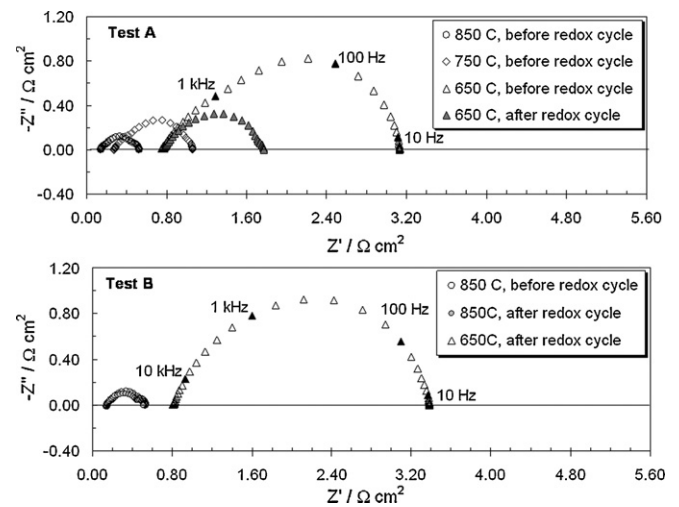

Fig. 10. Nyquist plots of representative impedance data recorded at OCV in 97% H_2 + 3% H_2O: at 850, 750 and 650 °C before re-oxidation and 10.2 h after the start of the re-reduction stage (test A, top); at 850 °C before re-oxidation, 850 °C at 10.2 h after the start of the re-reduction stage and 650 °C after the redox cycle (test B, bottom).
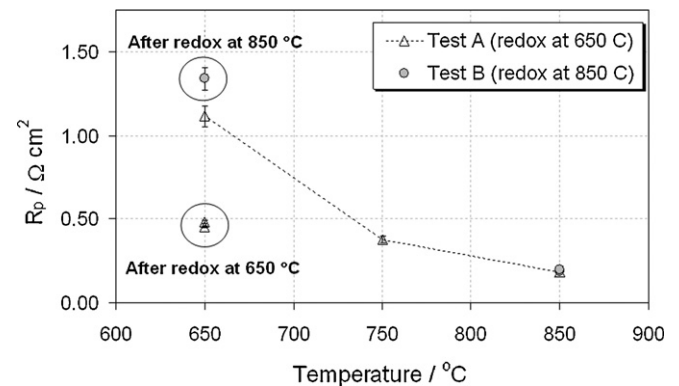

Fig. 11. Area specific polarisation resistance, R_p, as a function of temperature for test A, with a redox cycle performed at 650 °C, and test B, with a redox cycle performed 850 °C. Post-redox cycle values correspond to the measurements performed at 10.2 and 18.2 h into the re-reduction process.

of re-reduction at 650 °C the cell exhibits an R_p that is more than 60% lower than the starting value (before redox). The performance slightly deteriorates after 10.2 h, but no further significant changes can be seen from then on and up to 18.2 h of exposure to 97% H_2 + 3%
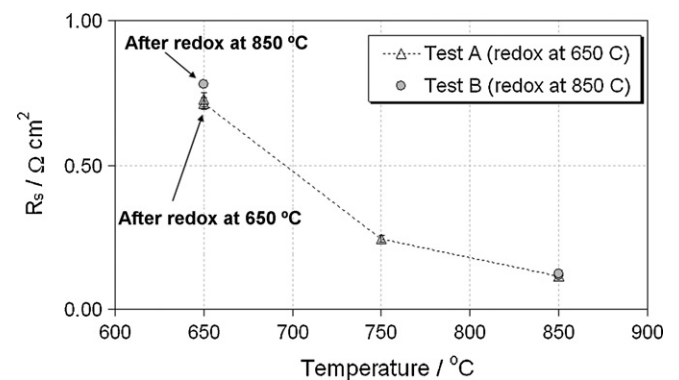

Fig. 12. Area specific series resistance, R_s, as a function of temperature for test A, with a redox cycle performed at 650 °C, and test B, with a redox cycle performed 850 °C. Post-redox cycle values correspond to the measurements performed at 10.2 and 18.2 h into the re-reduction process.
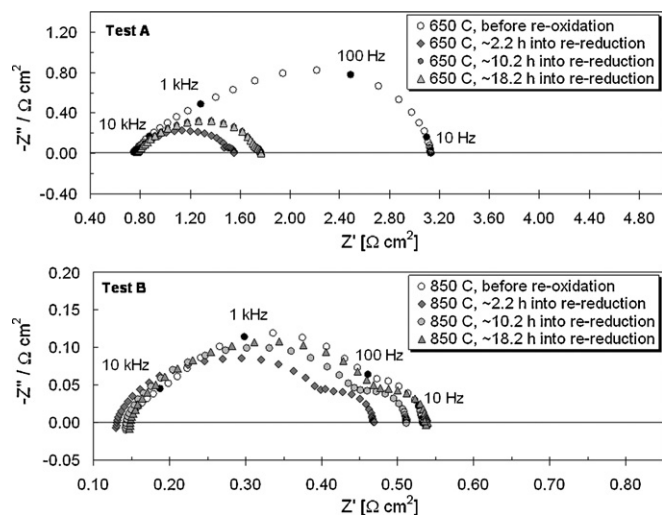
Fig. 13. Nyquist plots of impedance data obtained during test A or test B, exemplifying for one single cell changes in impedance spectra as a function of re-reduction time at 650 or 850 °C, after a re-oxidation period of 12 h at the same nominal temperature.

Fig. 14. Cross-section micrographs of representative symmetric cells after (a) reference test with fingerprinting between the nominal temperatures of 850–300 °C, (b) with redox cycle performed at the nominal temperature of 650 °C (test A) and (c) with redox cycle performed at the nominal temperature of 850 °C (test B).

H_2O. A small, but progressively increase of R_s can be seen with increasing re-reduction time. Analysing the impedance data for test B in a similar way, Fig. 13 shows that the impact of re-reduction time at 850 °C is very different. After a short exposure (~2.2 h) an improvement in R_p can be seen, although not as significant as that observed for test A at 650 °C. For this particular exposure time, a significant decrease in R_s is also seen. The performance improvement gradually disappears with further exposure time and, at 18.2 h, the pre-redox R_s and R_p values are approached.

Fig. 14 shows micrographs of tested cells after (a) the reference test performed between 850 and 300 °C, where they have not been subjected to a redox cycle, (b) after a redox cycle performed at 650 °C (test A) and (c) after a redox cycle performed at 850 °C (test B). All samples exhibit quite distinct microstructures and their impact on performance will be further evaluated and discussed. All samples were visually intact after testing.

4. Discussion

4.1. Ni-YSZ cermets

The operating conditions affect redox stability as was briefly discussed in the introduction. Additionally, the microstructure of the Ni-YSZ composite plays an equally important role as has been reported by several research groups and is very evident from the present data. We have identified the porosity of the sample as a major parameter affecting the dimensional stability in terms of both the CRS and DRR. The CRS after three isothermal redox cycles at 850 °C increases by a factor of more than 20 when the total porosity of the composite is reduced from 34 to 9%. For the same change in porosity the DRR reduces from 0.9–1 to 0.2–0.3. In light of the known effect from Ni sintering, the mechanism of redox instability and the impact of the re-oxidation temperature [21,22], the role of the porosity is to accommodate the volumetric expansion of the Ni phase when oxidised to NiO. The porosity dependence of CRS and DRR shown in Figs. 3–5 indeed shows that an increase in the porosity of the sample decreases the CRS on repeated redox cycles dramatically. Even though porosity is the single most important microstructural parameter affecting the dimensional stability, it is not the only one; others might be slightly masked by the effect from the total porosity. A closer examination of Figs. 4 and 5 shows that two of the high porosity samples ($p > 30\%$) exhibit a CRS_{max} above
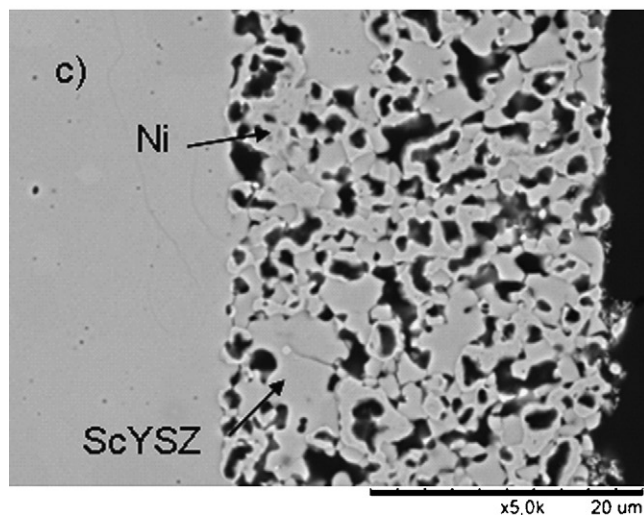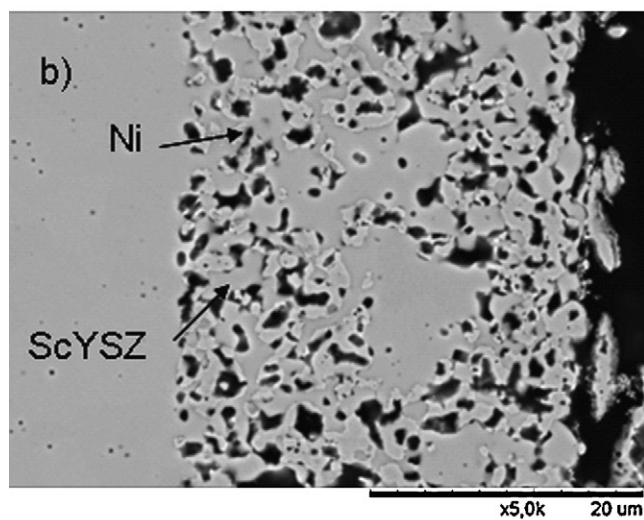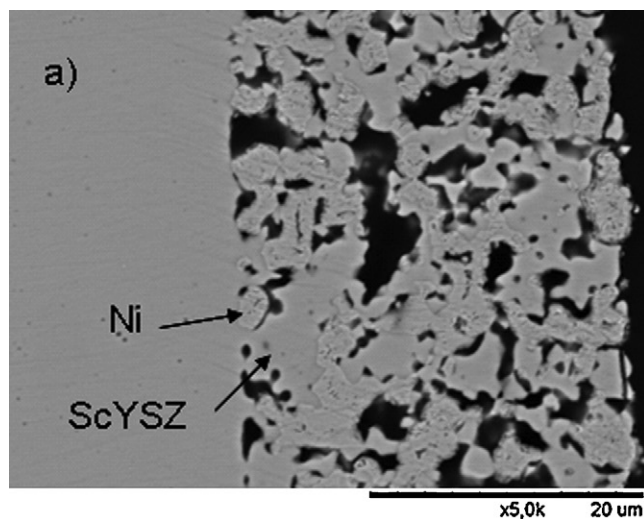
0.5% after the 3rd redox cycle, and lower DRR as compared with the rest of the high porosity samples. These samples could be identified as arising from the tape from which sample E was taken and a sibling tape of that, but sintered at a higher temperature than sample E. Possible effects from a higher sintering temperature include, besides the total porosity, the fraction of open porosity and the pore size distribution, as well as grain growth during sintering. Although no quantitative information on pore size distributions is presented here, the pore size distributions of the low and high porosity composites can be expected to be different so that the high total porosity samples have also a larger fraction of large pores.

Figs. 8 and 9 show the combined dilatometry-TGA results for the baseline and a modified composite, respectively, and give further insight into the dimensional behaviour of the cermets. The baseline cermet shows very little dimensional change upon the initial reduction at 850 °C, Fig. 8a, whereas the modified cermet exhibits a contraction of about 0.16% after an induction period of approximately 20 min; the DoO at this point into the reduction is about 0.35. As also discussed in [23], we believe this is related to the different relaxation behaviour of the Ni/NiO phase in the two composites. The initial reduction of the modified composite is considerably slower than of the baseline sample – full reduction is only reached after 5–6 h under reducing conditions. This means that even though the total porosity of the modified sample is higher than the baseline sample, the local microstructure in the NiO phase is different in a way that leads to slower reduction kinetics. As a comparison, the isothermal reduction time of the baseline sample is about 20 min. The stress relaxation in partially reduced Ni/NiO phase is much slower than in fully reduced Ni, therefore in the modified sample the reduction shrinkage of Ni is partially transformed into the ceramic backbone in the modified cermets and a bulk contraction during reduction is observed. On re-oxidation the baseline sample starts to show redox strain about 5 min after the change of the atmosphere into oxidising. This corresponds to about 0.4–0.5 in terms of DoO, Fig. 8b. The modified sample also shows an induction period of about 5 min until the re-oxidation strain appears, Fig. 9b. The rate of length change is, however, slower than for the baseline sample and the onset of expansion takes place at a higher DoO, about 0.8. It is noteworthy that the measured re-oxidation kinetics of the modified sample is faster than for the baseline sample. This could be due to the good access of air into the cermet through the high open porosity of the modified sample. Although the present data does not give the possibility to assess this, possibly also pathways for gaseous oxygen diffusion into the Ni-rich phase exist, e.g. through cracks of micro-fissures developing during the oxidation. As discussed in [23], the internal stresses in the NiO both from the oxidation process itself and the structural stresses arising from the expanding NiO-YSZ backbone can be several hundred MPa in magnitude.

One clear effect from the Ni doping on the cermets produced is the resulting variation in the as-sintered porosity. As was observed from the CRS and DRR variation of the undoped samples, the porosity variation directly affects the dimensional behaviour due to the different microstructures. The effect of the dopants on the actual sintering and redox behaviour of the Ni/NiO phase, if the microstructures were the same, is more difficult to assess directly due to the different porosities of the samples. We believe that the use of dopants is a potential way of tailoring cermets and improving the redox stability, but conclusive statements in this area require additional work. The effects of the dopants on the Ni sintering and electrical performance are an intended subject of a related paper.

4.2. Symmetric anode cells

The relation between anode polarisation resistances and redox stability with microstructure has long been established. Thus, in order to explain performance results the microstructures must be evaluated and compared. Fig. 14 shows micrographs of tested cells. It has been reported that successive redox cycles progressively decrease the NiO particle sizes [25] and that NiO particles formed from re-oxidation have a spongy-like structure with a higher-porosity than the as-sintered NiO [26]. If the reference cell (Fig. 14a) is directly compared to that of test A (Fig. 14b), redox cycled at 650 °C, the differences in microstructure are obvious. The cell from test A exhibits significantly smaller Ni particles and the presence of pores within the Ni grains can also be seen. It is known that highly dispersed fine grains of Ni and ceramic component in the cermet anode contribute to the increase of the triple phase boundary length (the electrochemical reaction area), thus leading to improved performances [27–30]. The microstructural changes seen for test A cells can thus justify the very large improvement seen in the polarisation resistances. On the other hand, the absence of visible cracks or particle detachment in the backbone and electrolyte integrity justify the very little variation seen in R_s for this test at the same nominal temperatures. The performance degradation observed during re-reduction can be attributed to Ni particle sintering and coarsening, with stable performances being reached after 10.2 h of re-reduction and up to 18.2 h of exposure. It is important to notice that, even though the performance decreased with time, the polarisation resistances at 10.2 h into the re-reduction period remained lower than the initial value by approximately 60%. Smaller Ni particles can also be seen for the test B cells (see Fig. 14c) when compared to the reference cell (Fig. 14a). However, the average size of the particles increased in comparison with that from test A, which have been subjected to a redox cycle at a significantly lower temperature. The different microstructure seen after cool down is possibly the combination of at least two factors. Firstly, higher re-oxidation temperatures lead to larger NiO particles [25], thus somewhat larger Ni grains on re-reduction could be expected. This fact can at least partly explain why the performance improvement seen after 2.2 h into the re-reduction is not as marked as seen for the 650 °C case. The improvement in R_s seen for this case is still not understood. However, it is possible that the phase reorganisation taking place during re-oxidation and initial stages of re-reduction could have improved the anode/electrolyte interfaces and originally inactive areas and/or areas with poor percolation were "recovered" in the new microstructural setup. Secondly, prolonged exposure to high temperatures is expected to increase both the rate and the extent of Ni sintering. This can justify the larger Ni particles and the higher degradation seen during the re-reduction period at 850 °C. Re-oxidation of the anode can lead to increased polarisation resistances due to crack formation within the anode [26]. A careful analysis of Fig. 14c reveals the presence several small cracks along the anode/electrolyte interface and what looks like the on-set of particle detachment in the ScYSZ backbone which, in addition to larger Ni grains, would explain the poorer performance (both in R_s and R_p) of these cells once measured at 650 °C (see Figs. 11 and 12). In comparison with the fingerprinting values, R_p increased from $1.12 \pm 0.06\ \Omega\,cm^2$ to $1.34 \pm 0.07\ \Omega\,cm^2$ and the R_s from $0.71 \pm 0.02\ \Omega\,cm^2$ to $0.80 \pm 0.01\ \Omega\,cm^2$. Higher re-oxidation temperature implies larger volume expansion, which in turn can affect the integrity of the backbone and electrolyte and ultimately, cause total mechanical failure of the cell [26]. Such drastic consequences have not been seen for the studied cells and, taking into account the exposure times, very high primary reduction temperature and harsh reduction conditions, the cells exhibited satisfactory redox stability. Summarising the results from the electrochemical tests, redox cycling at low temperatures seems to offer a potential means of improving anode performance or activating a degraded cell, provided that the redox cycling does not create damage in the ceramic backbone or interfaces. How durable the performance improvement is depends on the operation conditions after the re-reduction of the cell.

5. Conclusions

Different Ni-YSZ cermets were tested in dilatometry and thermogravimetry for dimensional stability during redox cycling under isothermal conditions at 850 °C. The dimensional stability was very dependent on the microstructure so that the samples with high porosity were the most stable. The cumulative redox strain, CRS_{max}, increased by a factor of more than 20 when the as-sintered porosity decreased from 34 to 9%.

The most stable cermets tested showed a maximum CRS_{max} not exceeding 0.1% during three redox cycles. Furthermore, the most stable cermets had a degree of redox reversibility, DRR, of nearly unity during the three isothermal redox cycles at 850 °C. In addition they were macroscopically intact after the experiments.

Electrochemical testing on Ni-ScYSZ symmetric cells showed that while isothermal redox cycling at 850 °C did not significantly alter the electrode performance, redox cycling of another cell with similar initial reduction treatment showed a 60% reduction in the polarisation resistance when redox cycled at 650 °C.

The improvement in the electrochemical performance of the anode on low temperature redox cycling was attributed to the change in the microstructure of the electrode due to the redox cycle. Smaller Ni grains and an undamaged ceramic structure were observed in the sample redox cycled at 650 °C.

References

[1] N.Q. Minh, T. Takahashi, Science and Technology of Ceramic Fuel Cells, Elsevier, Amsterdam, 1995.
[2] A. McEvoy, in: S.C. Singhal, K. Kendall (Eds.), High Temperature Solid Oxide Fuel Cells: Fundamentals, Design and Applications, Elsevier, 2003 (Chapter 6).
[3] A. Atkinson, S. Barnett, R.J. Gorte, J.T.S. Irvine, A.J. McEvoy, M. Mogensen, S.C. Singhal, J. Vohs, Nat. Mater. 3 (2004) 17–27.
[4] W.Z. Zhu, S.C. Deevi, Mater. Sci. Eng. A362 (2003) 228–239.
[5] H. Yokokawa, H. Tu, B. Iwanschitz, A. Mai, J. Power Sources 182 (2008) 400–412.
[6] D. Sarantaridis, A. Atkinson, Fuel Cells 7 (2007) 246–258.
[7] D. Sarantaridis, A. Atkinson, in: Proceedings of the 7th European SOFC Forum, Lucerne, Switzerland 2006, paper P0728.
[8] K. Kendall, C.M. Dikwal, W. Bujalski, ECS Trans. 7 (1) (2007) 1521–1526.
[9] C.M. Dikwal, W. Bujalski, K. Kendall, J. Power Sources 181 (2008) 267–273.
[10] A. Wood, M. Pastula, D. Waldbillig, D.G. Ivey, J. Electrochem. Soc. 153 (2006) A1929.
[11] S. Tao, J.T.S. Irvine, Nat. Mater. 2 (2003) 320–323.
[12] H. Itoh, T. Yamamoto, M. Mon, T. Horita, N. Sakai, H. Yokokawa, M. Dokiya, J. Electrochem. Soc. 144 (February (2)) (1997).
[13] D. Waldbillig, A. Wood, D.G. Ivey, Solid State Ionics 176 (2005) 847–859.
[14] D. Waldbillig, A. Wood, D.G. Ivey, J. Electrochem. Soc. 154 (2) (2007) B133–B138.
[15] T. Klemensø, PhD Thesis, Technical University of Denmark, 2005.
[16] J. Laurencin, G. Delette, F. Lefebvre-Joud, M. Dupeux, J. Eur. Ceram. Soc. 28 (2008) 1857–1869.
[17] A.N. Busawon, D. Sarantaridis, A. Atkinson, Electrochem. Solid-State Lett. 11 (10) (2008) B186–B189.
[18] D. Sarantaridis, R.A. Rudkin, A. Atkinson, J. Power Sources 180 (2008) 704–710.
[19] L. Grahl-Madsen, P.H. Larsen, N. Bonanos, J. Engell, S. Linderoth, J. Mater. Sci. 41 (2006) 1097–1107.
[20] J.L. Young, V. Vedahara, S. Kung, S. Xia, V.I. Birss, ECS Trans. 7 (1) (2007) 1511–1519.
[21] T. Klemensø, C. Chung, P.H. Larsen, M. Mogensen, J. Electrochem. Soc. 152 (11) (2005) A2186–A2192.
[22] M. Pihlatie, A. Kaiser, P.H. Larsen, M. Mogensen, J. Electrochem. Soc. 156 (2009) B322–B329.
[23] M. Pihlatie, A. Kaiser, M. Mogensen, Solid State Ionics, submitted for publication.
[24] M. Pihlatie, A. Kaiser, M. Mogensen, J. Eur. Ceram. Soc. (2008), doi:10.1016/j.jeurceramsoc.2008.10.017.
[25] Y. Zhang, B. Liu, B. Tu, Y. Dong, M. Cheng, Solid State Ionics 176 (2005) 2193–2199.
[26] B. Liu, Y. Zhang, B. Tu, Y. Dong, M. Cheng, J. Power Sources 165 (2007) 114–119.
[27] H. Abe, K. Murata, T. Fukui, W.-J. Moon, K. Kaneko, M. Naito, Thin Solid Films 496 (2006) 49–52.
[28] T. Fukui, K. Murata, S. Ohara, H. Abe, M. Naito, K. Nogi, J. Power Sources 125 (2004) 17.
[29] W. Guo, J. Liu, Solid State Ionics 179 (2008) 1516–1520.
[30] D.W. Dees, U. Balachandran, S.E Dorris, J.J. Heiberger, C.C. McPheeters, J.J. Picciolo, in: S.C. Singhal (Ed.), Solid Oxide Fuel Cells, PV 89-11, The Electrochemical Society Proceedings Series, Pennington, NJ, 1989, p. 317.